nature communications

Article

https://doi.org/10.1038/s41467-025-59547-y

Diminished biophysical cooling benefits of global forestation under rising atmospheric CO_2

Received: 5 December 2023

Accepted: 28 April 2025

Fei Kan[1], Hao Xu[1], Shuchang Tang[1], Josep Peñuelas[2,3], Xu Lian[1], Caspar T. J. Roebroek[4], Nazhakaiti Anniwaer[1], Kai Wang[1] & Shilong Piao[1]

Forestation is a proposed solution for mitigating global warming through carbon sequestration. However, its biophysical effects through surface energy modulation, particularly under rising CO_2 levels, is less understood. Here we investigate the biophysical effects of global potential forestation on near-surface air temperature (T_a) under increasing CO_2 concentrations using a land-atmosphere coupled model with slab ocean module. Our findings reveal that, under current climate conditions, the biophysical effect of global full-potential forestation can reduce land surface T_a by 0.062 °C globally. However, this cooling benefit diminishes as CO_2 rises. While elevated CO_2 slightly alters evaporative local cooling via stomatal closure and adjustments in forestation-driven rainfall regimes, the dominant reduction stems from non-local mechanisms. Background climate shifts reorganize forestation-induced horizontal temperature advection, weakening remote cooling in the Northern Hemisphere. These findings highlight the necessity of incorporating dynamic forest management strategies to optimize mitigation potential under a changing climate.

Forest's capacity of capturing and storing carbon through photosynthesis makes global forestation (afforestation and reforestation), an effective nature-based solution to curb climate change, complementing the efforts of greenhouse gas emission reduction[1–4]. Apart from its biochemical role in carbon cycling, forestation also affects local climate by directly modifying surface biophysical properties, such as albedo, roughness and evapotranspiration (ET)[5,6]. These biophysical feedbacks from forest change are often highly localized[7,8], driven by a latitudinal counteraction between the radiative warming effect resulting from reduced albedo (dominant in boreal regions) and the turbulent cooling effect via increased ET and surface roughness (predominant in tropical latitudes)[9–13]. The magnitude of these feedbacks also depends on transitions in vegetation types, as plant functional traits (PFTs) shape biophysical properties[11,14]. On a larger scale, forestation can impact climate non-locally by altering atmospheric circulations[10,15–19]. Recent observational and modeling studies have increasingly recognized that these remote temperature effects may surpass the local surface-driven effects[16,17,20]. In some regions, the combined local and non-local biophysical effects of forestation could rival or exceed its carbon sequestration benefits[21–25], highlighting the need for holistic assessments that integrate both aspects when investigating forestation's climate effects.

These biophysical effects are evolving with the ongoing rise of CO_2 concentrations[26–28]. Increasing CO_2 dynamically reshape forest biophysical properties and their local climate effects. For example, ET is influenced by both radiative and non-radiative CO_2 forcing: radiative

---

[1]Institute of Carbon Neutrality, Sino-French Institute for Earth System Science, College of Urban and Environmental Sciences, Peking University, Beijing 100871, China. [2]National Research Council of Spain (CSIC), Global Ecology Unit CREAF-CSIC-UAB, Bellaterra, Catalonia 08193, Spain. [3]Centre for Ecological Research and Forestry Applications (CREAF), Cerdanyola del Vallès, Catalonia 08193, Spain. [4]European Commission, Joint Research Centre (JRC), Ispra 21027, Italy. e-mail: xuhaotony@pku.edu.cn; slpiao@pku.edu.cn

forcing enhances surface net radiation and atmospheric vapor deficit, favoring energy-limited ET[29–31], while non-radiative effects involve two opposing mechanisms[32–34] – CO_2 fertilization effect, which enhances leaf area[35–37] and may increases transpiration, and the physiological effect, which reduces stomatal conductance[38,39], thus suppressing leaf-level water flux. Model simulations suggested that under high CO_2 levels, partial stomatal closure weakens the biophysical cooling effects of greening by reducing ET[28].

Elevated CO_2 can also influence atmospheric circulation through changes in sea surface temperatures (SSTs) and sea ice conditions (SICs). For instance, Arctic sea ice loss and amplified surface warming can weaken the meridional temperature gradient, altering large-scale meridional circulation[40–44], which may further influence the teleconnected climate impacts of afforestation. These CO_2-driven alterations in both local and non-local processes may fundamentally modulate the thermoregulation capacity of planted forests, altering their potential role in achieving carbon peak and neutrality goals. Therefore, it still remains an open question whether the contemporary biophysical feedbacks of forestation might be altered under future atmospheric CO_2 concentrations. Understanding the time-varying biophysical effects of forestation in response to elevated CO_2 is critical to the dynamic adjustment and optimization of climate mitigation strategies.

In this study, we conducted a series of equilibrium simulations using a coupled land-atmosphere climate model – the Institute Pierre Simon Laplace climate model (IPSL-CM)[45,46] – to explore the biophysical effects of global forestation on near-surface land air temperature (T_a) under rising CO_2 (see Methods). To better determine the implications of large-scale global forestation efforts for achieving "Net Zero", we applied an idealized scenario in which trees will be planted to the maximum potential of land-carrying capacity[47]. To better represent plausible trajectory of future CO_2 rise, we used three illustrative shared socioeconomic pathways (SSPs) beyond the current scenario – SSP1-2.6, SSP2-4.5, and SSP5-8.5, corresponding to low, medium, and high fossil fuel emission scenarios, respectively[48]. For each scenario, we conducted a pair of experiments that differ only in the prescribed PFTs maps: the forestation experiment (SCE) forced with full-potential tree cover map predicted by Bastin et al.[47], and the control experiment (CTL) forced with the current satellite-based PFT map[49]. Both simulations were run for 100 years under identical boundary conditions, with prescribed SSTs and SICs specific to rising CO_2 levels to minimize oceanic uncertainties. Although previous studies explored how forest changes affect land surface T_a through oceanic feedbacks[15,50], our focus is on the biophysical feedbacks of forestation through land-atmosphere interactions. The temperature difference between SCE and CTL quantifies the biophysical effects of global potential forestation on land surface T_a (hereafter denoted as ΔT_a) across different climate scenarios. Comparing these scenarios enables us to characterize how the biophysical effects of forestation evolve from current to future high CO_2 concentrations.

Results

Present cooling benefits of global forestation

We first examined the biophysical effects of global full-potential forestation under current CO_2 level (390 ppm; 1995–2014 observed mean). By comparing current and full-potential tree cover maps, we estimated that global land could support an additional 1.43 billion hectares (Bha) of tree cover (Bastin_Full in Fig. 1a). Hotspots of potential tree-planting (>20% tree cover gain) are concentrated in currently less vegetated regions, such as southeastern North America, eastern South America, Europe, Sahel, southeastern Asia and the periphery of the Congo rainforest.

Our model results show that globally, full-potential forestation could lead to a significant decrease in annual average T_a over land by −0.062 °C (Fig. 1e). This suggests an overall cooling effect of global forestation, but the value is relatively small due to the compensatory effect of regional cooling and warming across space (Fig. 1b). Significant decreases in T_a occur in regions with pronounced tree cover increase, including India, northeastern China, Europe, the Sahel, South Africa, eastern South America, and northern Australia. In contrast, forestation leads to net warming in high-latitudes regions, such as northeastern Siberia and northern Europe. It's interesting that notable temperature changes are also observed in regions with minimal tree cover gain (<2%), such as cooling over Eurasia, and warming over the Tibetan Plateau and Sahara. These remote temperature changes suggest that the large-scale forestation influences climate not only locally but also through teleconnected effects.

To further disentangle the drivers of forestation-induced temperature changes, we employed an analytical decomposition method[51] to separate the local effects from altered surface biophysical properties (ΔT_a^{local}) and non-local effects from atmospheric circulation changes (ΔT_a^{cir}). ΔT_a^{local} is the combined effect of changes in albedo (α), surface incoming shortwave radiation (S_{in}), air longwave radiative emissivity (ε_a), evapotranspiration (ET), and aerodynamic resistance (r_a), while ΔT_a^{cir} is defined as the residual in ΔT_a that is unexplained by above surface biophysical forcings (see Methods).

On a global average, local effects account for the major component of land surface air cooling, contributing −0.042 °C (Fig. 1c, e). Although ΔT_a^{local} dominates over only 33% of the land surface, it is the primary driver of ΔT_a in areas with substantial forestation, particularly in tropical and subtropical regions (Fig. 1c). The magnitude and direction of ΔT_a^{local} resulted from the competing effects of the five biophysical processes (i.e., α, S_{in}, ε_a, ET, r_a; Fig. 1e, Supplementary Figs. 1 and 2). Among these, enhanced ET is the strongest cooling factor, lowering T_a by −0.10 °C globally. However, this evaporative cooling is largely offset by surface albedo reduction[52], which increases absorbed solar radiation, producing a strong warming effect of +0.083 °C. It should be noted that, evaporative cooling acts solely on the land surface, whereas Δα-induced warming extends to the entire planet by reducing top-of-atmosphere (TOA) albedo and decreasing the amount of energy reflected back into space (Supplementary Fig. 3). The estimated effects of other biophysical processes (i.e., S_{in}, ε_a, and r_a) are smaller, yet statistically significant (Fig. 1e). ΔS_{in}-induced effect and $\Delta\varepsilon_a$-induced effect are the two complementary mechanisms caused by enhanced atmospheric water vapor and cloud cover[53–55] (Supplementary Fig. 4). Increased cloud reduces S_{in}, contributing a sizable cooling of −0.041 °C, while higher atmospheric water vapor increases ε_a and downward longwave radiation, warming the near-surface air by +0.063 °C (Fig. 1d). Additionally, reduced r_a in afforested areas – where forests replace short vegetation – facilitated the turbulent heat transfer from the land surface to the atmosphere boundary[13,56,57], leading to an additional cooling of −0.045 °C.

To ensure the robustness of our results from model simulations, we compared our estimated local biophysical effects against observation-driven studies employing space-for-time substitution[11,12,58]. This methodology quantifies land surface temperature differences (ΔT_s) between intact forests and neighboring non-forest counterparts, representing the local effects (ΔT_s^{local}) of full forest conversion on land surface temperature. We thus calculated the sensitivity of ΔT_s^{local} to tree cover change (i.e., ΔT_s^{local} due to 100% tree cover gain; Fig. 2). Both our model-based annual ΔT_s^{local} sensitivity and previous satellite-based studies[11,12,58] exhibit a latitudinal contrast: net warming in boreal regions versus cooling in tropical/subtropical regions (Fig. 2a, b). Seasonal analysis indicates that in northern high latitudes, albedo-driven warming is largely offset by the strong evaporative cooling from vigorous vegetation activity in summer (Fig. 2c, d), but is amplified in winter due to a greater reduction in snow-covered albedo (Fig. 2e, f). The strong agreement between our model-based findings and previous observational results in both latitudinal patterns and seasonal dynamics reinforce the reliability of our estimated local biophysical effects.

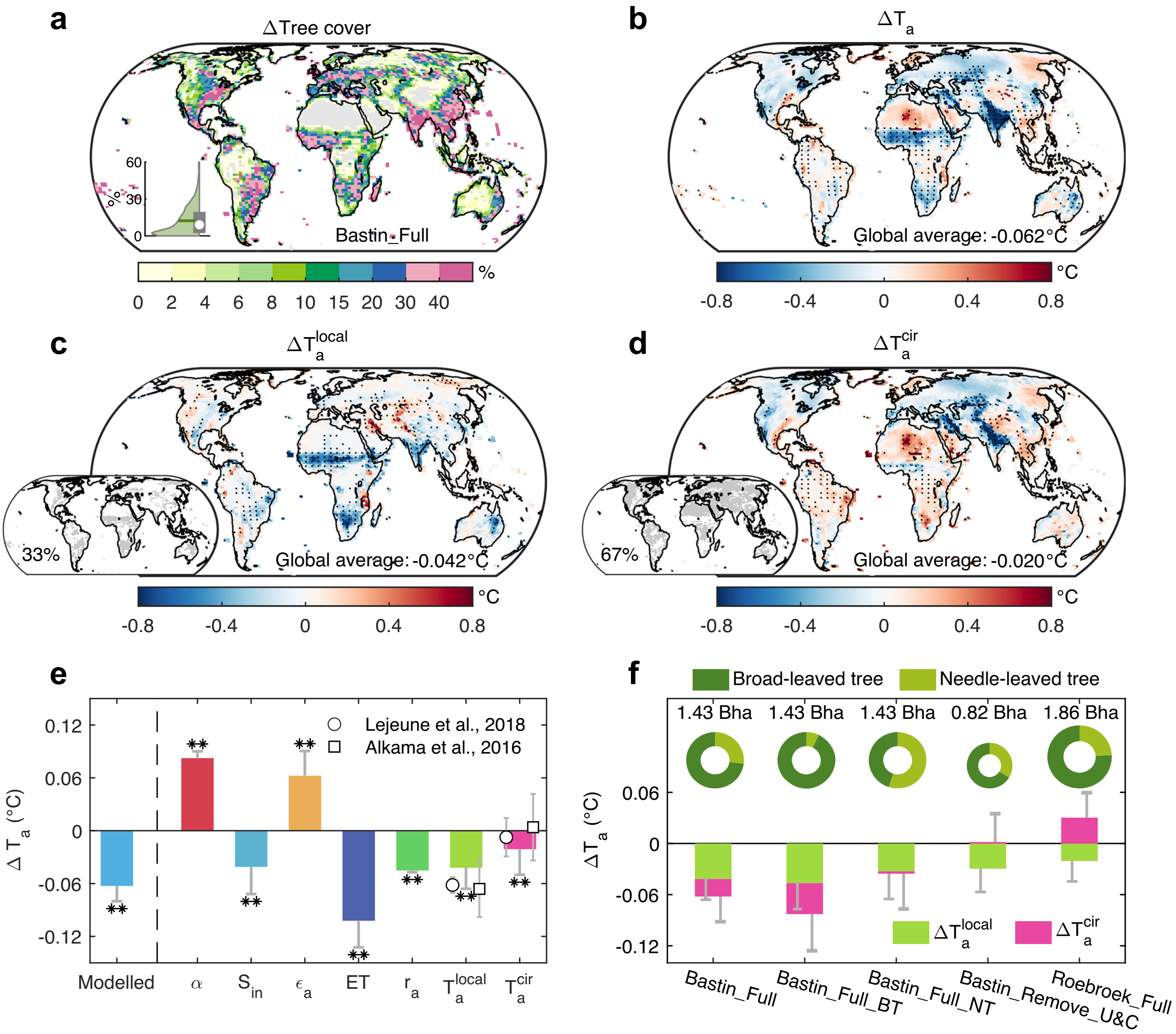

Fig. 1 | Biophysical effects of global potential forestation on near-surface air temperature (T_a) under current climatic conditions. **a** Geographical pattern of tree fraction changes (ΔTree cover) resulting from full-potential forestation based on Bastin et al.' data[47] (Bastin_Full). The inserted half violin plot displays the density, median (horizontal line), mean (circle), 25th, 75th quartiles of ΔTree cover. **b** Geographical pattern of forestation-induced T_a changes (ΔT_a). **c**, **d** Geographical pattern of ΔT_a related to altered surface properties (ΔT_a^{local}, **c**) and atmospheric teleconnections (ΔT_a^{cir}, **d**). The insets below **c** and **d** indicate the regions where ΔT_a is dominated by ΔT_a^{local} or ΔT_a^{cir}. Black stipples in **b**, **c** and **d** denote statistically significant temperature change using Student's t-test and Benjamini-Hochberg correction at the 5% significance level. **e** Global average of forestation-induced ΔT_a and contributions of ΔT_a^{local} and ΔT_a^{cir}. ΔT_a^{local} consists of five sub-components associated with changes in albedo (α), downward shortwave radiation (S_{in}), air emissivity (ε_a), evapotranspiration (ET) and aerodynamic resistance (r_a), respectively. The estimates of ΔT_a^{local} and ΔT_a^{cir} by two additional methods from Lejeune et al.[59] and Alkama et al.[12] are shown as circles and squares, respectively. Error bars indicate the 1-standard deviation of the last 40-year series. $^{**}p < 0.05$; $^{*}p < 0.1$. **f** The impact of different potential forestation forcings on modeled ΔT_a. Besides the Bastin_Full scenario in the main text, we considered four additional scenarios: maximum broad-leaved tree forestation (Bastin_Full_BT), maximum needle-leaved tree forestation (Bastin_Full_NT), forestation excluding urban and croplands (Bastin_Remove_U&C), all of which are based on Bastin et al.'s data, and full-potential forestation from Roebroek et al.'s data[60] (Roebroek_Full). The rings at the top show the total forestation area (the ring size and the text above the ring) and the mean canopy composition ratios of planted trees (broad-leaved trees/needle-leaved trees).

Global forestation also exerts far-reaching remote impacts by reorganizing large-scale atmospheric circulation[10,16,17,50]. The global mean land surface T_a response to teleconnected feedbacks is relatively weak ($\Delta T_a^{cir} = -0.021$ °C; Fig. 1e). However, non-local effects dominate the combined ΔT_a over 67% of the land surface at the grid-cell scale, particularly in areas with minimal tree planting (Fig. 1d). ΔT_a^{cir} manifests as a widespread surface air cooling in northern mid-to-high latitudes, where it outweighs the weak local warming (positive ΔT_a^{local}) in Eurasia and North America, whereas it amplifies existing local cooling (negative ΔT_a^{local}) in India and northeastern China (Fig. 1c, d). Conversely, in tropical regions, ΔT_a^{cir} induces a warming that partially offsets local cooling, particularly in the Amazon Basin, southern Africa, Southeast Asia (Fig. 1c, d). Notably, the spatial pattern of ΔT_a^{cir} and its dominant role across the Northern Hemisphere (NH) are nearly consistent with the multi-model ensemble results from Coupled Model Intercomparison Project phase 6 (CMIP6) Earth System Models (ESMs) (Supplementary Fig. 5; see Methods).

To validate our surface energy budget method, we applied two alternative methods to isolate ΔT_a^{local} and ΔT_a^{cir} without further decomposing specific processes. These include the linear

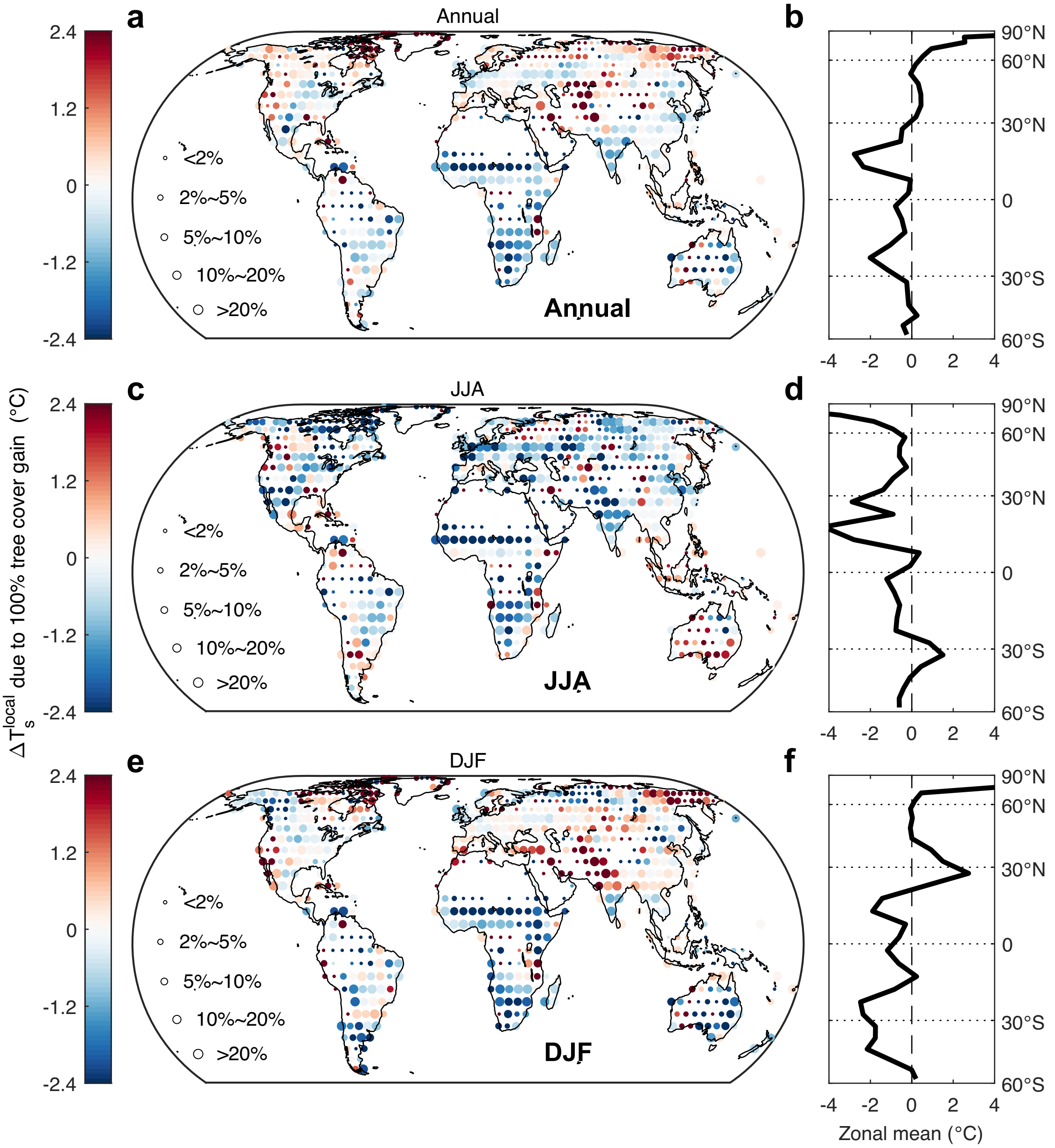

Fig. 2 | Land surface temperature changes from local biophysical effect (ΔT_s^{local}) due to full-potential forestation under current climatic conditions. a, c, e Geographical patterns of annual mean (**a**), JJA (June-July-August, **c**) and DJF (December-January-February, **e**) ΔT_s^{local} due to global forestation. The symbol size indicates the magnitude of tree cover gains, and the color specifies the average temperature sensitivity to total forestation. Points are spaced 5° in both latitude and longitude, and statistics were computed in windows measuring 15° by 15°. **b, d, f** Zonal averages of the annual mean (**b**), JJA (**d**), and DJF (**f**) ΔT_s^{local} statistics at 5° of latitudinal resolution.

regression method following Lejeune et al.[59] and the inverse distance weighted interpolation method as per Alkama et al.[12] (see Supplementary Text 1). Both methods yield local and non-local effect magnitudes that support our findings based on our surface energy budget method, despite minor differences in spatial patterns (Supplementary Fig. 6) and global mean values (markers in Fig. 2e).

In the forestation scenarios described above, the proportions of different tree types in newly established trees were determined based on their current distribution ratios. Considering that future tree species preferences could influence the magnitude of climate feedback effects, we developed two idealized scenarios under the full-potential forestation condition in the current climate: prioritizing the planting of broad-leaved trees (Bastin_Full_BT) or prioritizing the planting of needle-leaved trees (Bastin_Full_NT) (Supplementary Fig. 7). Compared to the Bastin_Full scenario, which maintains the current tree type distribution, the broad-leaved tree-dominated scenario (Bastin_Full_BT) exhibits a stronger local cooling ($\Delta T_a^{local} = -0.047$ °C; Fig. 1f). In contrast, needle-leaved tree-dominated scenario (Bastin_Full_NT) produces a reduced local cooling ($\Delta T_a^{local} = -0.033$ °C; Fig. 1f). This divergence is most pronounced in northern mid-to-high latitudes, where the differences in canopy composition are largest (Supplementary Figs. 7 and 9a, c). Our finding is consistent with observed evidence that broad-leaved trees tend to exert a stronger evaporative cooling effect compared to needle-leaved trees[11,14].

To assess the sensitivity of biophysical temperature responses to the spatial extent and geographic locations of the planted trees, we consider two alternative forestation scenarios: a more realistic forestation scenario (Bastin_Remove_U&C) based on Bastin et al.'s data[47] by excluding urban and agricultural lands (Supplementary Fig. 8a), and another full-potential forestation scenario (Roebroek_Full) using alternative tree cover capacity dataset from Roebroek et al.[60] (Supplementary Fig. 8b). In the Bastin_Remove_U&C scenario, the reduced forestation area weakens global local cooling ($\Delta T_a^{local} = -0.030$ °C; Fig. 1f), particularly across Africa, India, and eastern China (Supplementary Figs. 8a and 9e). However, the Roebroek_Full scenario, with a larger global forestation potential, yet shows weaker local cooling globally ($\Delta T_a^{local} = -0.020$ °C; Fig. 1f). This is because Roebroek et al.'s estimates suggest a greater forestation potential in high-latitude regions such as Europe, where the higher estimates yield minimal changes on local effects of weak cooling or warming. Meanwhile, lower estimates of forestation potential in tropical and subtropical regions, such as Africa and western India, weaken local cooling effects of forestation (Supplementary Figs. 8b and 9g).

Across these four sensitivity scenarios with varying forestation forcings, the responses of atmospheric circulation to forestation exhibit greater uncertainties, with the varied magnitudes and even the signs of global mean ΔT_a^{cir} (ΔT_a^{cir} in Fig. 2f and Supplementary Fig. 9). The inconsistent ΔT_a^{cir} responses across scenarios further drives divergent net temperature changes (ΔT_a) due to forestation globally (combined ΔT_a^{local} and ΔT_a^{cir} in Fig. 2f). However, all scenarios consistently support our findings in the Bastin_Full baseline scenario, that local effects dominate the biophysical feedbacks in afforested regions, particularly in the tropics; while non-local effects prevail in non-afforested regions, especially across northern mid-to-high latitudes (Supplementary Fig. 9).

Diminished cooling benefits with rising CO_2

To investigate how the current biophysical cooling benefits of global forestation may evolve under elevated CO_2 concentrations, we include three additional illustrative future scenarios: SSP1-2.6 (low), SSP2-4.5 (medium), and SSP5-8.5 (high emission pathways). The CO_2 concentrations of the three scenarios are set as the projected end-of-century (2081-2100) mean: 460ppm, 600ppm, 1000ppm, respectively (see Methods). Our model estimates indicate that under the low-emission SSP1-2.6 scenario, the biophysical cooling benefits of full-potential forestation on the land surface T_a is −0.059 °C – only slightly weaker than that under present-day climate conditions. However, as CO_2 concentrations increase, this cooling benefit diminishes, reaching merely −0.035 °C and −0.021 °C under the medium-emission SSP2-4.5 and high-emission SSP5-8.5 scenarios, respectively. This attenuation is primarily driven by diminished non-local cooling (increasing ΔT_a^{cir}) under elevated CO_2 (discussed further in the next section). In contrast, the local cooling effects exhibit different responses across rising CO_2: they slightly weaken (increased ΔT_a^{local}) under SSP1-2.6 and SSP2-4.5 scenarios, marginally contributing to reduced biophysical cooling, whereas they strengthen (decreased ΔT_a^{local}) under SSP5-8.5 scenario, becoming decoupled from the overall cooling decline.

Mechanistic analysis identifies ΔET-induced cooling as the dominant driver of ΔT_a^{local} responses under rising CO_2 (Fig. 3b). Forestation-induced ET enhancement declines under SSP1-2.6 and SSP2-4.5 scenarios, but increases under SSP5-8.5 scenario. This ΔET responses can be approximately explained by the CO_2-mediated shift in forestation-driven precipitation changes (Fig. 3c). To gain further insights into radiative and non-radiative CO_2 effects on forestation-induced ΔET, we applied the Budyko framework to partition ΔET into contributions from changes in potential evapotranspiration (PET), land surface properties, and precipitation (Supplementary Text 2 and Supplementary Fig. 10). The PET-derived ET component, representing CO_2 radiative effects, shows negligible changes under high CO_2. In contrast, the land surface-driven ET component, reflecting CO_2 non-radiative effects, reveals a pronounced suppression of forestation-induced ET enhancement under elevated CO_2. This suppression results from the dominance of stomatal closure (reducing ΔET) over the combined effect of CO_2 fertilization and warming-driven lengthening of the growing season (increasing ΔET). However, CO_2-induced adjustments in precipitation-driven ΔET partially or even completely offset this physiological suppression, particularly under SSP5-8.5 scenario.

The cooling effect associated with Δr_a (reduced aerodynamic resistance) represents the second-largest magnitude among CO_2-driven responses, intensifying with rising CO_2 (Fig. 3b). This is because CO_2 fertilization enhances the climatological leaf area index (CTL LAI, Fig. 3d), increasing vegetation roughness and facilitating turbulent transfer. In this rougher environment, tree-planting can more efficiently cool near-surface air through turbulent transfer. Therefore, despite a slight decrease in forestation-induced r_a reduction (negative Δr_a), the substantial reduction in overall forest r_a (CTL r_a) leads to diminished r_a-associated cooling effects under elevated CO_2 levels. The impacts of elevated CO_2 on ΔT_a caused by the other three surface radiative attributes are relatively small (Fig. 3b). Specifically, the $\Delta\alpha$ (reduced surface albedo)-induced warming effect weakens marginally with the rise in CO_2, linked to diminishing background snow cover (CTL snow fraction) under future warming, which reduces forestation-induced albedo decreases (Fig. 3e). ΔS_{in} (reduced downward shortwave radiation)-induced cooling is often completely counteracted by $\Delta\varepsilon_a$ (increased air emissivity)-induced warming, primarily due to forestation-driven enhancements in cloud cover that modulate their covariation (Fig. 3f). These mechanisms collectively demonstrate that CO_2-modulated background states critically regulate local biophysical effects of forestation.

Temperature advection driving the CO_2-mediated non-local effects responses

Given the dominance of non-local effects (ΔT_a^{cir}) in shaping forestation-induced biophysical responses under elevated CO_2, we further elucidated the mechanisms underlying CO_2-modulated atmospheric teleconnection responses. Global forestation indeed induces remarkable changes in winds over land, leading to non-local atmospheric temperature alterations (Supplementary Figs. 11–13). Temperature changes at 850 hPa, the interface between the atmospheric troposphere and the surface boundary layer, closely align with ΔT_a in spatial pattern (comparing Fig. 1b and Supplementary Fig. 13a). To better understand these responses, we analyzed horizontal temperature advection changes (ΔT_{adv}) at 850 hPa, decomposing them into zonal (ΔT_{adv}^u, driven by zonal wind changes Δu) and meridional (ΔT_{adv}^v, driven by meridional wind changes Δv) components.

At current CO_2 levels, ΔT_{adv} provides a reasonable explanation for non-local atmospheric feedback induced by forestation (Fig. 4a). Particularly across the mid-to-high latitudes of the Northern Hemisphere (NH), global afforestation can trigger a stationary Rossby wave train, forming anomalous high-pressure centers over the Scandinavian Peninsula and the Bering Strait (Supplementary Fig. 14a). This dynamic perturbation alters large-scale atmospheric circulation (Supplementary Figs. 11a and 12a), leading to widespread non-local cooling across Eurasia and North America (Fig. 4a). Over Eurasia, the substantial cooling stems from significantly attenuated westerlies and northward winds (negative Δu and Δv; Fig. 4c, e and Supplementary Figs. 11a, 12a). Under climatological background conditions (CTL), prevailing westerlies facilitate warm air advection from Europe, while northward winds transport warm air from lower latitudes (Supplementary Fig. 15). Reduced westerlies and northward flows thus suppress these heat influxes (negative ΔT_{adv}^u and ΔT_{adv}^v; Fig. 4c, e), driving Eurasian non-local cooling. A similar dual-pathway advective cooling governs North America, where weakened eastward advection of warm air from the west, combined with enhanced southward intrusion of cold air from the Arctic (Fig. 4c, e and Supplementary Figs. 11a, 12a, 15).

We further focus on how NH ΔT_{adv} responds to increasing CO_2 concentrations, to explore the diminished cooling benefits driven by the changes in non-local effects (bars in Fig. 4b), Our analysis reveals that the increasing ΔT_{adv} can also approximately explains the

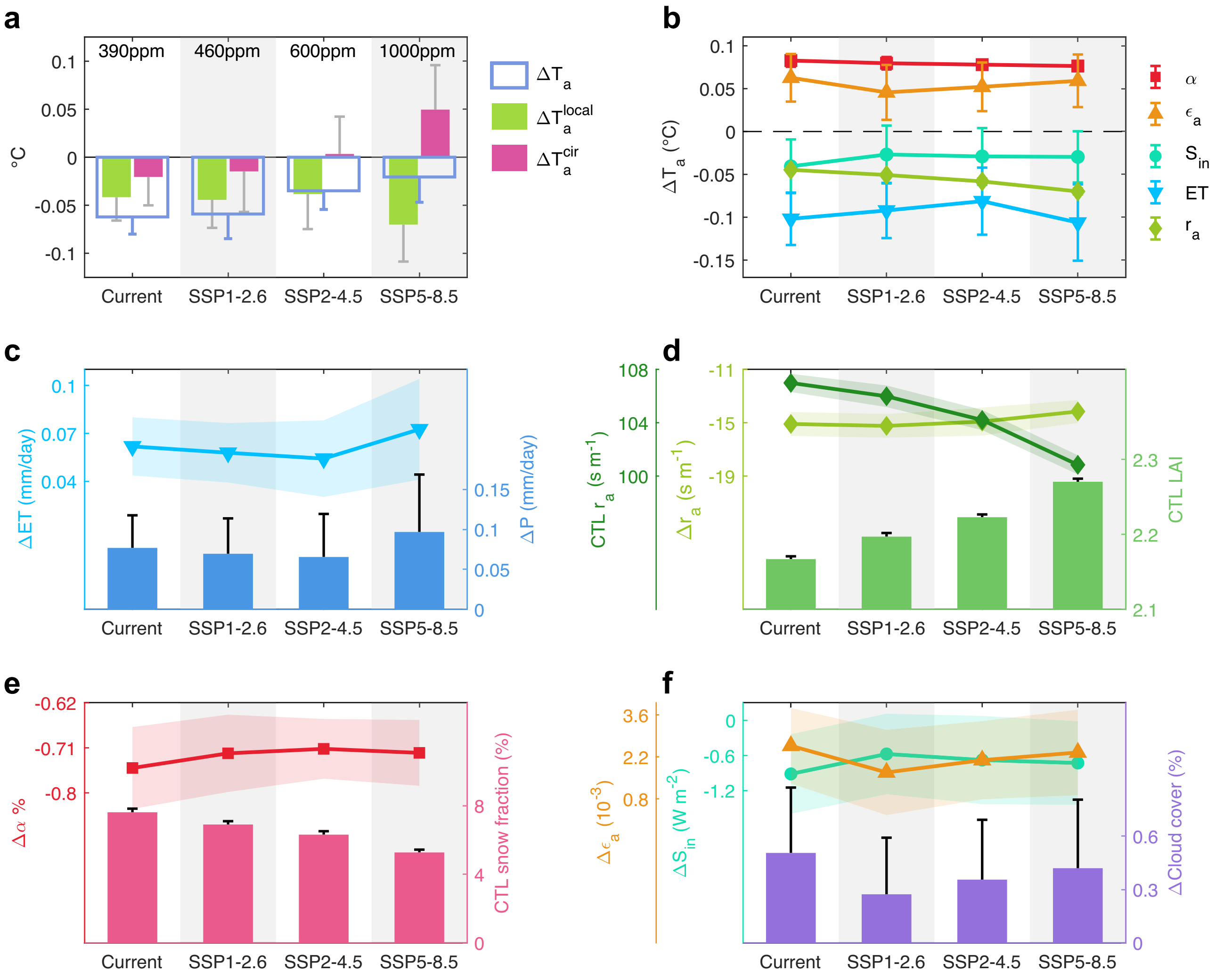

Fig. 3 | The response of near-surface air temperature change (ΔT_a) induced by the biophysical feedback of global forestation to rising CO_2. **a** Global average of forestation-induced ΔT_a, and its two components associated with altered surface properties (ΔT_a^{local}) and atmospheric teleconnections (ΔT_a^{cir}) under rising CO_2 (Current: 390 ppm; SSP1-2.6: 460 ppm; SSP2-4.5: 600 ppm; SSP5-8.5: 1000 ppm). **b** Global average of forestation-induced ΔT_a as a function of rising CO_2, associated with changes in the five surface biophysical processes, including surface albedo (α), surface incoming shortwave radiation (S_{in}), air emissivity (ε_a), evapotranspiration (ET), and aerodynamic resistance (r_a). **c** Global average of forestation-induced changes in ET (ΔET, curve) and precipitation (ΔP, bars) under rising CO_2. **d** Global average of forestation-induced changes in r_a (Δr_a, curve), climatological r_a (CTL r_a, curve), and climatological leaf area index (CTL LAI, bars) under rising CO_2. **e** Global average of forestation-induced changes in α (curve) and climatological snow cover (CTL snow cover, bars) under rising CO_2. **f** Global average of forestation-induced changes in S_{in} (ΔS_{in}, curve), ε_a ($\Delta \varepsilon_a$, curve), and cloud cover (ΔCloud cover, bars) under rising CO_2. The shaded area of the curves and the error bars of bars indicate the uncertainty ranges (1-standard deviation of the last 40-year runs).

weakening non-local cooling effects across the NH (Fig. 4b). Forestation-induced wind alterations (Δu and Δv) in response to rising CO_2 concentrations shape the evolution of corresponding directional ΔT_{adv} (ΔT^u_{adv} and ΔT^v_{adv}) under CO_2 forcing (Fig. 4d, f). While zonal wind-driven advection responses remain variable (Δu and ΔT^u_{adv} in Fig. 4d), the meridional wind component (Δv) and associated thermal advection (ΔT^v_{adv}) exhibit an overall upward trend with rising CO_2 concentrations, emerging as the primary driver underpinning the increasing ΔT_{adv} (Fig. 4f). This meridional dominance may arise from CO_2-induced modifications of the atmospheric background state. Elevated CO_2 drives Arctic amplification through dramatic Arctic sea ice loss and surface warming[61,62]. This process reduces both meridional temperature gradients and barometric pressure differentials, thereby diminishing meridional air advection[41,43,44,63]. The alterations in climatic background further interact with forestation-caused atmospheric teleconnections, shifting the propagation of global forestation-triggered Rossby waves and the formation of high-pressure anomalies (SSP5-8.5 as an example in Supplementary Fig. 14b). Consequently, the potential of global forestation to cool the land surface air across the NH by regulating meridional temperature advection is weakened, ultimately leading to diminished biophysical cooling.

Discussion

In this work, we reveal the potential of global full-forestation to lower the land surface air temperature globally by −0.062 °C through biophysical feedbacks under current climatic conditions (Fig. 1). Local effects due to direct land surface changes contribute most to this global cooling benefit. Tropical afforestation regions witness the strongest local cooling effects, primarily driven by the cooling from increased ET. While atmospheric teleconnections exert minimal influence on global mean land surface T_a, their non-local effects surpass local effects in regions with limited tree-planting. Particularly across northern mid-to-high latitudes, forestation-induced changes in zonal and meridional circulation drive pronounced non-local cooling via altered horizontal temperature advections (Fig. 4).

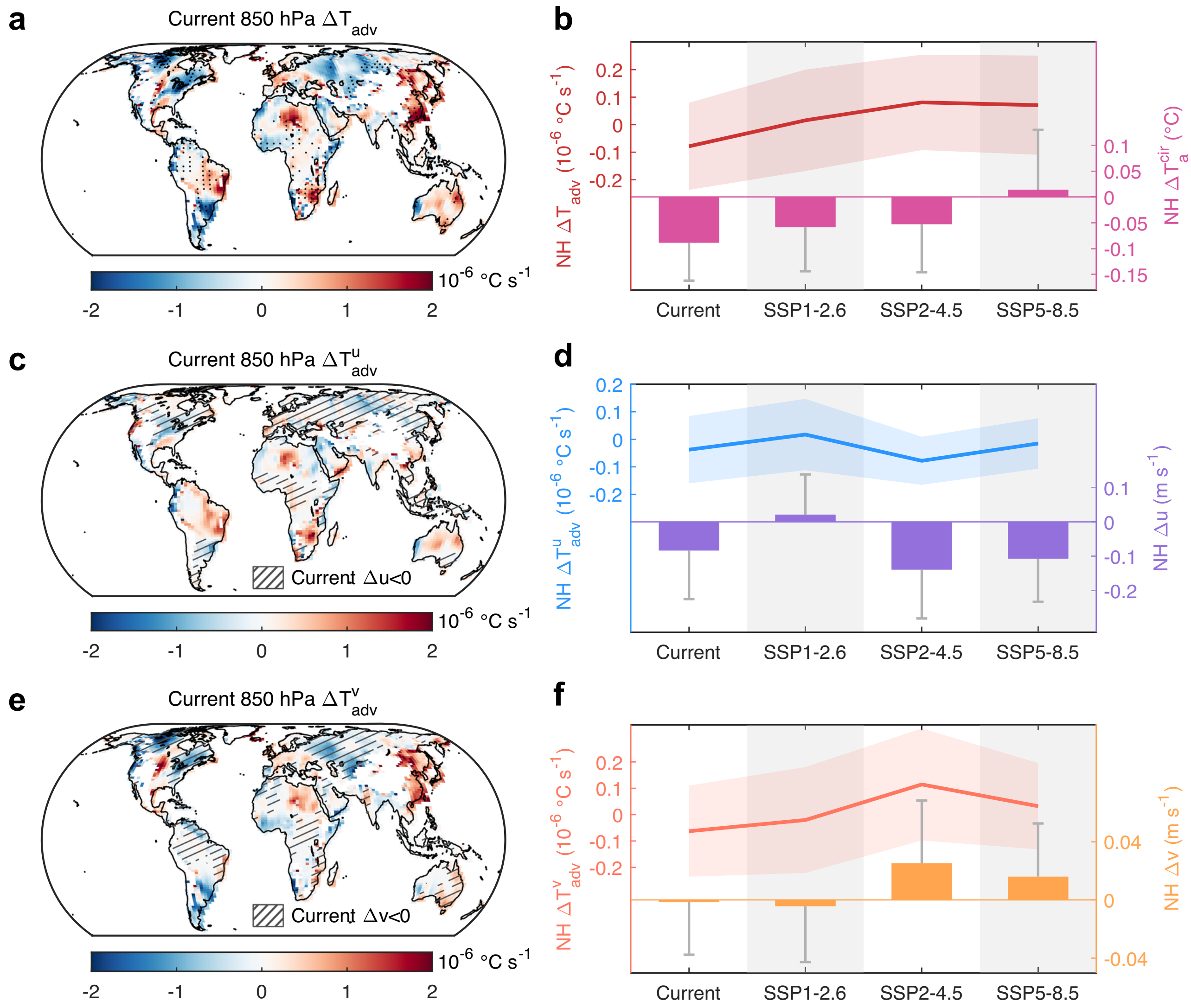

Fig. 4 | Altered temperature advection driving regional atmospheric teleconnections and its dynamic response to rising CO_2 levels. a, **c**, **e** Geographical pattern of forestation-induced changes in 850 hPa total (ΔT_{adv}, **a**), zonal (ΔT^u_{adv}, **c**) and meridional (ΔT^v_{adv}, **e**) horizontal temperature advection, respectively, at current CO_2 level. Black stipples in **a** denote statistically significant temperature change using Student's t-test and Benjamini-Hochberg correction at the 5% significance level. The hatched area in **c** and **e** indicates where global forestation suppresses 850 hPa westerlies ($\Delta u < 0$) and northward winds ($\Delta v < 0$), respectively. **b** The evolution of ΔT_{adv} (curve) and teleconnected air temperature changes (ΔT_a^{cir}, bars) across the Northern Hemisphere (NH) under rising CO_2 levels. **d**, **f** The evolution of zonal (**d**) and meridional (**f**) wind component (Δu, Δv; bars) and associated temperature advection (ΔT^u_{adv}, ΔT^v_{adv}; curves) across the NH under rising CO_2 levels. The shaded area of curves and the error bars of bars indicate the uncertainty ranges (1-standard deviation of the last 40-year runs).

However, as atmospheric CO_2 levels continue to rise, the biophysical cooling benefits of global forestation gradually diminish (Fig. 3), depending on modifications in climatic background states induced by high CO_2 levels. For local biophysical effects, elevated CO_2 suppresses stomatal conductance, thereby reducing the ΔET-driven evaporative cooling. Nevertheless, this physiological forcing is partially or even completely counterbalanced by adjustments in forestation-induced precipitation changes under high CO_2 levels (Supplementary Fig. 10). Regarding atmospheric feedbacks, CO_2-enriched Arctic amplification perturbs NH meridional circulation, potentially weakening the non-local cooling caused by modified cold/warm air advection (Fig. 4). Crucially, the diminished non-local cooling constitutes the primary pathway for CO_2-driven decline in the cooling benefits of forestation (Fig. 3).

The pronounced teleconnected feedbacks in the NH align with earlier modeling studies demonstrating that non-local effects dominate over local biophysical impacts of forest cover changes in northern mid-to-high latitudes[16–18]. CMIP6 muti-model ensemble further substantiate the primacy of atmospheric feedback mechanisms in shaping NH biophysical responses (Supplementary Fig. 5). This atmospheric dominance suggests that observation-based space-for-time substitution approaches, while capable of capturing small-scale processes, may introduce significant biases in assessing forest change feedbacks due to their failure to account for teleconnections[20]. For instance, while observational studies suggest that afforestation in Eurasia induces minimal cooling or even net warming through albedo effects[11,58], our simulations and CMIP6 muti-model ensemble demonstrate substantial cooling caused by the non-local feedbacks of global large-scale forestation. These atmospheric teleconnections can further indirectly influence land surface temperature through the coupling between surface temperature and air temperature[64]. In addition to temperature effects, forestation-induced atmospheric feedback may alter precipitation both locally and remotely through reorganizing large-scale circulation patterns, such as the Hadley circulation[15,65,66]. Therefore, we highlight the imperative to integrate atmospheric feedbacks into the evaluation of large-scale forestation strategies.

Nevertheless, current ESMs show substantial uncertainties in simulating teleconnected responses compared to local effects. Model discrepancies emerge in both magnitude and sign of global mean ΔT_a^{cir} (Supplementary Fig. 5), potentially stemming from divergent atmospheric physics parameterizations. This finding aligns with previous studies, which demonstrated that the non-local effects of forest cover changes explain the discrepancies in biophysical effects across different climate models[17,64]. The characteristics of forestation forcing, including location, scale and canopy composition, further modulate these teleconnections (Fig. 1f and Supplementary Fig. 9). These uncertainties are particularly evident across NH mid-to-high latitudes, possibly due to the enhanced activity of poleward Rossby waves caused by subtropical-midlatitude forcing in these regions[67,68]. Prioritizing constraints on atmospheric feedback uncertainties across modeling frameworks may be a key focus for advancing climate mitigation assessments. We also urge the Earth system modeling community to verify the response of atmospheric feedback to elevated CO_2 by incorporating future scenario with an identical afforestation map in experiments.

Beyond land surface teleconnections, global afforestation triggers atmospheric feedbacks that indirectly modulate atmospheric temperatures over oceans, particularly in the upper-level troposphere (Supplementary Fig. 13). Such atmospheric temperature perturbations could theoretically propagate into sea surface temperature anomalies, potentially altering ocean circulation and generating further teleconnections[15]. However, our study excludes such ocean-atmosphere coupling feedbacks, focusing instead on atmospheric circulation responses driven exclusively by land surface modifications. Even within this constrained framework, these non-local mechanisms dominate the biophysical impacts of forestation across northern mid-to-high latitudes. Incorporating ocean dynamics would introduce higher-uncertainty teleconnected effects through coupled ocean-atmosphere interactions, which would further obscure the surface process-driven local feedbacks central to our investigation. While using a slab ocean module could potentially reduce uncertainties from oceanic processes, the capacity of land-use changes to perturb ocean circulation[15,50] underscores the need for future comprehensive assessments of the climate impacts of global afforestation using fully coupled Earth system models.

Our model-based results indicate that future changes in the climatic background will diminish the cooling benefits of forestation under elevated CO_2 concentrations. Moreover, increased wildfire frequency, intensifying extreme events, and prolonged droughts under climate change could further erode the cooling benefits of afforestation. Notably, CO_2-induced alterations in climatic background not only affect the potential benefits of future afforestation, but may also undermine the climate mitigation capacity of existing natural forests and plantations. The impacts of rising CO_2 on biophysical feedbacks of land-use changes may be larger than that on biochemical feedbacks[24,69]. We therefore propose implementing dynamic and climate-adaptive management strategies in large-scale afforestation programs to better achieve carbon neutrality. Besides, the suppressive effect of high CO_2 on forestation-induced biophysical cooling necessitates integrating nature-based afforestation strategies concurrently with efforts of greenhouse gas emission reduction (e.g., renewable energy systems), to maximize the biophysical cooling benefits by lowering atmospheric CO_2 concentrations.

Methods

Equilibrium experiments with a coupled land-atmosphere model

In this study, we used the IPSL-CM coupled land-atmosphere climate model (1.26° × 2.5°) to simulate the biophysical effects of potential global tree restoration on air temperature under equilibrium climate conditions. IPSL-CM was developed by the Institute Pierre Simon Laplace modeling community and has participated in the Coupled Model Intercomparison Project (CMIP) phases 5 and 6[45,46]. It consists of two main components that have been updated to the latest version: the Laboratoire de Météorologie Dynamique atmospheric general circulation model with zooming capability (LMDZ, version 5, v2076) and the Organizing Carbon and Hydrology in Dynamic Ecosystems (OCHIDEE, v3035) land surface model. LMDZ characterizes atmospheric physical dynamics and processes such as convection, boundary layer, and cloud[70,71], while OCHIDEE describes water and energy balance, vegetation, and soil carbon cycle in terrestrial ecosystems[72]. The OCHIDEE model divides terrestrial plant function types (PFTs) into 13 categories, including 12 vegetation types and one bare ground type, each with independent parameters to calculate total vegetation physiological processes. The IPSL-CM has been widely used to quantify the biophysical impacts of vegetation changes on temperature and the hydrological cycle[10,51,73,74], for its outstanding performance in simulating key vegetation-related processes, including the ratio of vegetation-driven transpiration to the evapotranspiration, T/ET[75].

The biophysical feedbacks of forestation on near-surface air temperature (T_a) are isolated by a pair of equilibrium experiments with the carbon cycle module deactivated. The two sets of experiments differed solely in their prescribed PFT conditions: the “CTL” run was forced with current PFT maps, whereas the “SCE” run was prescribed with the hypothesized PFT maps with global forestation to the full of ecosystems’ potential[47]. Land cover dynamics were excluded from the model configuration to isolate the climatic response attributable exclusively to the prescribed forestation forcing. To investigate the impacts of future rising CO_2 on the biophysical feedbacks of forestation, we conducted this experiment pair under both the current CO_2 concentration and the projected CO_2 concentrations of three illustrative future scenarios. The current atmospheric CO_2 concentration was set at 390 ppm, representing the average value of observed concentrations during the historical period (1995–2014)[76]. The three representative future scenarios are SSP1-2.6, SSP2-4.5, and SSP5-8.5, corresponding to low, medium, and high fossil fuel emission pathways, respectively[48]. The CO_2 concentrations for each future scenario were based on the projected average values for the late 21st century (2081–2100), with specific values of 460 ppm, 600 ppm, and 1000 ppm, respectively[77]. The CO_2 concentration data were derived from the CMIP6 historical and SSP scenario forcing datasets constructed by Meinshausen et al.[76,77]. Each equilibrium experiment was run for 100 years. We used the last 40 years of monthly output data for further analysis because the simulations typically reached an equilibrium state in around 60 years. Each of the last 40 years could be regarded as an independent run under the equilibrium state. The 40-years data allowed us to estimate the uncertainty in forestation biophysical response.

The current land cover map was from the 2020 global PFT map provided by the European Space Agency’s Climate Change Initiative (ESA CCI)[49]. The ESA CCI global annual PFT maps are derived from the existing 300 m medium-resolution land cover product of the ESA CCI, integrated with additional high-resolution remote-sensing observations (e.g., the products of tree canopy, tree canopy height, and surface water). This product has been verified in two land surface models − ORCHIDEE and the Joint UK Land Environment Simulator (JULES). Compared with the generic cross-walking table, this product has made remarkable improvements in the fractions of trees, short vegetation, and bare-soil cover. Following the ORCHIDEE model guidelines (https://orchidas.lsce.ipsl.fr/dev/lccci/description.php), we converted the 14 ESA CCI PFTs into the 13 PFTs required by ORCHIDEE, incorporating Köppen-Geiger climate zones and C3/C4 grass and crop ratios. Notably, as ORCHIDEE lacks a dedicated shrubland category, shrubland PFTs in the original ESA CCI classification were reallocated to tree- and grass-related PFTs based on the proportion of forests and grasslands.

The potential tree cover across the globe was derived from Bastin et al.[47]. Bastin et al. developed a random forest machine-learning model to extrapolate tree cover measurements from protected areas to the globe using satellite-observed environmental conditions[47]. In the forestation scenario (Bastin_Full), the tree cover increases from current to potential levels was assigned to different tree types using their current fraction (used in the CTL run) as the weighting factor. This allocation principal ensured that the dominant tree type increased most substantially in the SCE run. In addition, different definition and classification methods of forest among data sources or overfit of the machine learning models might lead to greater tree cover of the current level than the potential level. In such cases, we assigned the tree cover in the SCE run as that in CTL run, suggesting no afforestation attempts. There is a total of 8 tree PFTs in our model: tropical broad-leaved evergreen, tropical broad-leaved raingreen, temperate needleleaf evergreen, temperate broad-leaved evergreen, temperate broad-leaved summergreen, boreal needleleaf evergreen, boreal broad-leaved summergreen, boreal needleleaf summergreen. The 1.43 Bha forestation potential differs slightly from Bastin et al.'s reported 1.6 Bha[47], as we updated the tree cover map to 2020 for the CTL scenario.

The land-atmosphere coupling model does not incorporate the ocean module, which help reduce potential biases propagated from oceanic processes. However, this model cannot fully capture the effects of rising CO_2 on land surface temperature through altering sea surface temperatures (SSTs) and sea ice concentration (SICs) changes. To better reproduce the future T_a predicted by the global climate models (GCM), SSTs and SICs were prescribed to align with the scenario-specific CO_2 concentration levels. For the current CO_2 concentration, SSTs and SICs were prescribed as the observed averages during the historical period (1995–2014). The observational data were sourced from the input datasets of the Model Intercomparison Project, which integrates observational products from the UK Met Office Hadley Centre and the optimally interpolated reanalysis products from the National Oceanic and Atmospheric Administration (NOAA). For the CO_2 concentrations under the three future SSP scenarios, we bias-corrected the SST and sea ice outputs from the Scenario Model Intercomparison Project (ScenarioMIP)[48] of CMIP6 using observational data. For each SSP scenario, we first calculated the multi-model mean changes in SSTs and SICs for the late 21st century (2081–2100) relative to the historical period (1995–2014). These projected changes were then added to the observed historical averages (1995–2014) to derive the bias-corrected SSTs and SICs for the late 21st century. This bias-correction approach reduces potential large deviations in the model-projected SSTs and SICs at the end of the century. The use of 20-year averages was adopted to minimize the influence of natural variability modes on SST and SIC anomalies. Here, we adopted the average values of the available outputs from 26 CMIP6 ESMs, including ACCESS-CM2, ACCESS-ESM1-5, BCC-CSM2-MR, CAMS-CSM1-0, CanESM5, CanESM5-1, CAS-ESM2-0, CESM2-WACCM, CMCC-CM2-SR5, CMCC-ESM2, EC-Earth3, EC-Earth3-Veg, EC-Earth3-Veg-LR, FGOALS-f3-L, FGOALS-g3, GFDL-ESM4, INM-CM4-8, INM-CM5-0, IPSL-CM6A-LR, MIROC6, MPI-ESM1-2-HR, MPI-ESM1-2-LR, MRI-ESM2-0, NorESM2-LM, NorESM2-MM, TaiESM1.

The analytical decomposition of forestation-induced T_a changes

To gain a better mechanistic understanding of the forestation-induced T_a changes, we analytically decomposed the temperature effects following the same methodology of Zeng et al.[51]. This decomposition method enables disentangling the two dominant components driving the T_a changes: (1) local impacts of surface biophysical processes through directly perturbing land-atmosphere energy exchange, ΔT_a^{local} and (2) non-local impacts due to changes in air advection on small scales or atmospheric circulation on large scales, ΔT_a^{cir}. Hence, the overall T_a changes induced by global tree restoration can be written as:

$$\Delta T_a = \Delta T_a^{local} + \Delta T_a^{cir} \tag{1}$$

ΔT_a^{local} associated with the forestation-induced alterations in surface processes is estimated based on the land-surface energy budget at land-surface layer. The land-surface energy balance is given by:

$$S_{in} - S_{out} + L_{in} - L_{out} = \lambda E + H + G \tag{2}$$

where S_{in} and S_{out} denote surface downward and upward shortwave radiation, respectively. L_{in} and L_{out} denote surface downward and upward shortwave radiation, respectively. λE represents the latent heat flux, where λ is the latent heat of vaporization and E is evapotranspiration (ET). H is the sensible heat flux and G is the ground flux, which can be neglected due to its small magnitude on seasonal and longer timescales. Among them, S_{in} is indirectly impacted by forestation-induced changes in cloud, while E can be directly enhanced by forestation. S_{out}, L_{in}, L_{out} and H need to be further decoupled using empirical formulas, to identify the key variables that respond to surface processes.

S_{out} is given as:

$$S_{out} = \alpha S_{in} \tag{3}$$

where α is the surface albedo, which is calculated using the model outputs of S_{in} and S_{out}. Tree-planting can reduce α directly.

L_{in} and L_{out} are estimated by:

$$L_{in} = \sigma \varepsilon_a T_a^4 \tag{4}$$

$$L_{out} = \varepsilon_s L_{in} + \sigma \varepsilon_s T_s^4 \tag{5}$$

where σ is the Stephan-Boltzmann constant (5.67×10^{-8} W m^{-2} K^{-4}), ε_a and ε_s are the air longwave radiative emissivity and land surface emissivity, respectively. As most of atmospheric water vapor is confined near the surface, we used the model outputs of land surface L_{in} and T_a at 2 m height to derive near-surface ε_a. Similar to S_{in}, ε_a is driven by forestation-induced changes in atmospheric water vapor and clouds. Note although ε_s also varies with land cover, soil moisture, and snow cover, we here consider it as a constant value of 0.95 for simplicity. This is because the ε_s obtained from satellite observations does not vary significantly over most vegetated surfaces, and it differs slightly from 0.95 across different land cover layers.

H is given as:

$$H = \rho C_d \frac{T_s - T_a}{r_a} \tag{6}$$

where ρ, C_d denote air density (1.21 kg m^{-3}) and specific heat capacity of air at constant pressure (1,013 J kg^{-1} K^{-1}). r_a is the aerodynamic resistance at 2 m height, which is directly provided by model output. Similar to α and E, increasing tree cover can directly reduce r_a to facilitate turbulent transfer.

Combining Equations (2)–(6), the surface energy balance budget is expanded into the following form:

$$S_{in}(1-\alpha) + \varepsilon_s \sigma \left(\varepsilon_a T_a^4 - T_s^4 \right) = \lambda E + \rho C_d \frac{T_s - T_a}{r_a} \tag{7}$$

In the process above, we have identified five key surface biophysical processes driven by afforestation, including albedo (α), surface incoming shortwave radiation (S_{in}), air longwave radiative emissivity

(ε_a), evapotranspiration (ET or λE) and aerodynamic resistance (r_a). The alterations in these surface processes can further modulate T_s. Among them, S_{in}, E, r_a can be obtained from the model output, while α and ε_a are derived based on Equations (3) and (4), respectively, using the model output variables.

Assuming that the other variables (i.e., σ, ε_s, λ, ρ, C_d) are all independent of T_s. we further differentiate Equation (7) with respect to T_s, giving the expressions for ΔT_s:

$$\Delta T_s = \frac{1}{f_s}\left[-S_{in}\Delta\alpha + (1-\alpha)\Delta S_{in} + \varepsilon_s\sigma T_a^4\Delta\varepsilon_a - \lambda\Delta E + \frac{\rho C_d(T_s - T_a)}{r_a^2}\Delta r_a\right] + \frac{\rho C_d/r_a + 4\varepsilon_s\sigma\varepsilon_a T_a^3}{\rho C_d/r_a + 4\varepsilon_s\sigma T_s^3}\Delta T_a \tag{8}$$

where f_s is the energy redistribution factor for T_s, representing the sensitivity of land surface warming to 1 W m^{-2} radiative forcing, given by:

$$f_s = \frac{\rho C_d}{r_a} + 4\varepsilon_s\sigma T_s^3 \tag{9}$$

On the right-hand side of Eq. (8), the first term denotes the afforestation-driven T_s changes caused by the altered surface radiative forcing ($\Delta T_s^{local} = \frac{1}{f_s}\left[-S_{in}\Delta\alpha + (1-\alpha)\Delta S_{in} + \varepsilon_s\sigma T_a^4\Delta\varepsilon_a - \lambda\Delta E + \frac{\rho C_d(T_s - T_a)}{r_a^2}\Delta r_a\right]$), and the second term denotes the direct impact of T_a on T_s. This strong land-atmosphere coupling indicates that radiative changes of T_s can further drive the changes of T_a ($\Delta T_a^{local} = \frac{\rho C_d/r_a + 4\varepsilon_s\sigma T_s^3}{\rho C_d/r_a + 4\varepsilon_s\sigma\varepsilon_a T_a^3}\Delta T_s^{local}$). Combining Equation (1) and (8), we can obtain the expression of ΔT_a as:

$$\Delta T_a = \frac{1}{f_a}\left[-S_{in}\Delta\alpha + (1-\alpha)\Delta S_{in} + \varepsilon_s\sigma T_a^4\Delta\varepsilon_a - \lambda\Delta E + \frac{\rho C_d(T_s - T_a)}{r_a^2}\Delta r_a\right] + \Delta T_a{}^{cir} \tag{10}$$

where f_a is the energy redistribution factor for T_a, given by:

$$f_a = \frac{\rho C_d}{r_a} + 4\varepsilon_s\sigma\varepsilon_a T_a^3 \tag{11}$$

On the decomposition of ΔT_a, $-S_{in}\Delta\alpha$, $(1-\alpha)\Delta S_{in}$, $\varepsilon_s\sigma T_a^4\Delta\varepsilon_a$, $-\lambda\Delta E$ and $\frac{\rho C_d(T_s - T_a)}{r_a^2}\Delta r_a$ represents the forestation-induced radiative forcing changes through altering surface biophysical processes (i.e., α, S_{in}, ε_a, ET, r_a). These forcings form the radiative component of T_a changes on local scale (ΔT_a^{local}), and the residual component denotes non-local T_a changes caused by altering atmosphere circulation (ΔT_a^{cir}).

Multi-model Validation Based on the CMIP6 ESMs

To verify the robustness of our model-based results, we isolate the biophysical feedbacks of potential afforestation using two sets of simulations from CMIP6: the Shared Socioeconomic Pathway 3-7.0 scenario simulation (SSP3-7.0) of the Scenario Model Intercomparison Project (ScenarioMIP)[48] and the future land-use policy sensitivity simulation (SSP3-7.0 - SSP1-2.6Lu) of the Land Use Model Intercomparison Project (LUMIP)[78]. The SSP3-7.0 - SSP1-2.6Lu simulation is identical to SSP3-7.0 except that land use and land cover changes (LULCCs) are derived from the Shared Socioeconomic Pathway 1-2.6 scenario (SSP1-2.6), which involves with substantial afforestation or reforestation primarily in the tropics (Supplementary Fig. 5a). The last 30 years simulations (2071–2100) for SSP3-7.0 and SSP3-7.0 - SSP1-2.6Lu were compared (SSP3-7.0 - SSP1-2.6Lu minus SSP3-7.0) to isolate the biophysical effect of afforestation.

Next, we separated forestation-induced ΔT_a^{local} and ΔT_a^{cir} based on the surface energy balance method. Notably, abundant observation-based evidence indicates that tropical afforestation can cool the land surface due to the dominant evaporative cooling effect. This forestation-induced biophysical cooling benefit in the tropics is projected to continue in the future[24,25,27]. In total, eight models satisfy this constraint and produce the output variables required by the surface energy balance method: ACCESS-ESM, CNRM-ESM2-1, IPSL-CM6A-LR, MPI-ESM1-2-LR, BCC-CSM2-MR, MIROC-ES2L, NorESM2-LM and UKESM1-0-LL.

Four sensitivity experiments with different potential-forestation map

Firstly, considering that different planted tree types may affect the biophysical impact of tree planting, we tested the effect on our results of maintaining the same overall afforestation area but varying the tree species. Here we developed two additional idealized scenarios based on the full-potential forestation data from Bastin et al.: (1) Bastin_Full_BT, where broad-leaved trees are planted wherever possible; and (2) Bastin_Full_NT, where needle-leaved trees are planted wherever possible. Unlike the Bastin_Full scenario, which implements afforestation according to the proportion of CTL tree PFTs, these two scenarios exclusively use local broad-leaved tree PFTs and needle-leaved tree PFTs for forestation. If there are no broad-leaved tree PFTs or needle-leaved tree PFTs in the CTL for a given grid cell, it is assumed that the environment does not support the broad-leaved trees or needle-leaved trees. In this case, consistent with the Bastin_Full scenario, afforestation is implemented according to the proportion of the CTL tree PFTs. In the Bastin_Full scenario, global afforestation mainly increases broad-leaved trees, primarily in tropical regions and NH mid-to-low latitudes (Supplementary Fig. 7a). In contrast, the increase in needle-leaved trees mainly occurs in the NH mid-to-high latitudes (Supplementary Fig. 7b). In the Bastin_Full_BT scenario, broad-leaved trees are planted in all areas where the environment supports additional tree cover increase, except for a few Arctic regions, such as northeastern Siberia and northern Canada, where needle-leaved trees are planted (Supplementary Fig. 7c, d). Conversely, in the Bastin_Full_NT scenario, among the areas that support additional forestation, broad-leaved trees are only planted in tropical and subtropical regions, while needle-leaved trees are planted in boreal and temperate regions (Supplementary Fig. 7e, f). Globally, these two scenarios have different canopy composition ratios (broad-leaved trees/needle-leaved trees) of forestation from that of the Bastin_Full (Bastin_Full: 73:27; Bastin_Full_BT: 92:8; Bastin_Full_NT: 45:55; Fig. 1f).

Secondly, we considered a more realistic potential afforestation scenario by excluding afforestation on croplands and urban areas (Bastin_Remove_U&C), based on the potential tree cover data from Bastin et al. and the ESA CCI global land cover map for 2020. In this scenario, additional 0.85 Bha trees are planted beyond the urban and agricultural lands (Fig. 1f). Compared to the Bastin_Full scenario, the loss of forestation potential in the Bastin_Remove_U&C scenario predominantly occurs in Europe, India, southeastern China, southeastern North America, eastern South America, and the Sahel (Supplementary Fig. 8a).

Thirdly, we included another full-potential forestation scenario using data provided by Roebroek et al.[60] (Roebroek_Full) to verify the robustness of our dataset. Similar to the commonly used data from Bastin et al.[47], the authors predicted the tree cover carrying capacity by integrating satellite-based observations of tree cover within a machine learning framework. However, they utilized the concept of integrated disturbance regimes and thus developed a data that are more closely aligned with tree cover observations in the intact areas, such as the

Congo rainforest. Additionally, this dataset has the advantages of a higher R^2 and lower spatial variance. In contrast, compared to the data from Bastin et al.[47], it provides a low estimate of the afforestation potential in arid ecosystems, for example, in South Africa and western India (Supplementary Fig. 8b). On a global average, the Roebroek_Full scenario has a larger forestation potential, covering an area of 1.85 Bha (Fig. 1f).

It should be noted that, considering the availability of computational resources, these four sensitivity experiments were all conducted only under the current CO_2 concentration. Given the dominant role of NH non-local effects in driving forestation-induced biophysical feedbacks under current climatic conditions (Fig. 1d and Supplementary Fig. 9) − and their control over the dynamic response to rising CO_2 levels in Bastin_Full scenario (Fig. 4b), it can be inferred that CO_2-driven climatic background state modifications will similarly modulate biophysical feedbacks across all four sensitivity scenarios through influencing NH non-local effects.

Non-local effect attributed to near-surface horizontal temperature advection

In this study, we chose to calculate the forestation-induced changes in temperature advection at the 850 hPa, because 850 hPa is a commonly used atmospheric isobaric surface closest to the Earth's surface. The formula for calculating horizontal temperature advection is as follows:

$$T_{adv} = T^{u}_{adv} + T^{v}_{adv} = \left(-u\frac{dT}{dx}\right) + \left(-v\frac{dT}{dy}\right) \tag{12}$$

where T_{adv}, T^{u}_{adv}, T^{v}_{adv} represent total, zonal ($-u\frac{dT}{dx}$), and meridional ($-v\frac{dT}{dy}$) temperature advections (°C s^{-1}) at 850 hPa, respectively. u, v, T represent zonal wind (m s^{-1}), meridional wind (m s^{-1}) and atmospheric temperature (°C) at 850hpa, respectively. $u > 0$ denotes eastward wind, and $v > 0$ denotes northward wind. $\frac{dT}{dx}$ and $\frac{dT}{dy}$ represent zonal and meridional temperature gradient, respectively. Using the u, v, T output in CTL and SCE, we can obtain global forestation-induced ΔT_{adv}, ΔT^{u}_{adv}, ΔT^{v}_{adv} based on Equation (12). For a grid cell, ΔT_{adv} (or ΔT^{u}_{adv}, ΔT^{v}_{adv}) > 0 denotes that more warm air or less cold air is transported to this grid cells from the nearby region.

Data availability

All data used for our numerical simulations in this study are publicly available. The 2020 PFT map from European Space Agency's Climate Change Initiative (ESA CCI) is available at https://doi.org/10.5285/26a0f46c95ee4c29b5c650b129aab788. The datasets mapping the global tree restoration potential are from Bastin et al. (https://doi.org/10.1126/science.aax0848) and Roebroek et al. (https://doi.org/10.1038/s41597-025-04408-y), respectively. Both datasets are available on request. The historical and future CO_2 concentrations dataset for climate modeling is available at the supplementary information of ref. 77 (https://doi.org/10.5194/gmd-13-3571-2020). The datasets mapping historical and future SSTs and SICs are available at https://esgf-node.llnl.gov/projects/input4mips/. The model outputs of SSP3-7.0 and SSP3-7.0 - SSP1-2.6Lu scenarios supporting our findings are available at https://esgf-node.llnl.gov/projects/input4mips/. Source data for all figures are available at https://doi.org/10.6084/m9.figshare.28596668.

Code availability

Code and documentation for the IPSL-CM model are publicly available at https://cmc.ipsl.fr/ipsl-climate-models/ipsl-cm5/. Model outputs were processed using the software Matlab 2023a. The analysis scripts are available at https://doi.org/10.6084/m9.figshare.28596668.

References

1. Canadell, J. G. & Raupach, M. R. Managing forests for climate change mitigation. *Science* **320**, 1456–1457 (2008).
2. IPCC. *Climate change 2021: The physical science basis. contribution of working group I to the sixth assessment report of the intergovernmental panel on climate change* (eds Masson-Delmotte, V. et al.) (Cambridge University Press, 2021).
3. Griscom, B. W. et al. Natural climate solutions. *Proc. Natl Acad. Sci. USA* **114**, 11645–11650 (2017).
4. Lewis, S. L., Wheeler, C. E., Mitchard, E. T. A. & Koch, A. Restoring natural forests is the best way to remove atmospheric carbon. *Nature* **568**, 25–28 (2019).
5. Bonan, G. B. Forests and climate change: Forcings, feedbacks, and the climate benefits of forests. *Science* **320**, 1444–1449 (2008).
6. Davin, E. L. & De Noblet-Ducoudré, N. Climatic impact of global-scale deforestation: radiative versus nonradiative processes. *J. Clim.* **23**, 97–112 (2010).
7. Pitman, A. J. et al. Importance of background climate in determining impact of land-cover change on regional climate. *Nat. Clim. Change* **1**, 472–475 (2011).
8. Li, Y. et al. The role of spatial scale and background climate in the latitudinal temperature response to deforestation. *Earth Syst. Dynam.* **7**, 167–181 (2016).
9. Peng, S.-S. et al. Afforestation in China cools local land surface temperature. *Proc. Natl Acad. Sci. USA* **111**, 2915–2919 (2014).
10. Li, Y., Piao, S., Chen, A., Ciais, P. & Li, L. Z. X. Local and teleconnected temperature effects of afforestation and vegetation greening in China. *Natl Sci. Rev.* **7**, 897–912 (2020).
11. Duveiller, G., Hooker, J. & Cescatti, A. The mark of vegetation change on earth's surface energy balance. *Nat. Commun.* **9**, 679 (2018).
12. Alkama, R. & Cescatti, A. Biophysical climate impacts of recent changes in global forest cover. *Science* **351**, 600–604 (2016).
13. Lee, X. et al. Observed increase in local cooling effect of deforestation at higher latitudes. *Nature* **479**, 384–387 (2011).
14. Schwaab, J. et al. Increasing the broad-leaved tree fraction in European forests mitigates hot temperature extremes. *Sci. Rep.* **10**, 14153 (2020).
15. Portmann, R. et al. Global forestation and deforestation affect remote climate via adjusted atmosphere and ocean circulation. *Nat. Commun.* **13**, 5569 (2022).
16. Chen, L. & Dirmeyer, P. A. Reconciling the disagreement between observed and simulated temperature responses to deforestation. *Nat. Commun.* **11**, 202 (2020).
17. Winckler, J., Lejeune, Q., Reick, C. H. & Pongratz, J. Nonlocal effects dominate the global mean surface temperature response to the biogeophysical effects of deforestation. *Geophys. Res. Lett.* **46**, 745–755 (2019).
18. Winckler, J. et al. Different responses of surface temperature and air temperature to deforestation in climate models. *Earth Syst. Dynam.* **10**, 473–484 (2019).
19. De Hertog, S. J. et al. The biogeophysical effects of idealized land cover and land management changes in Earth system models. *Earth Syst. Dynam.* **13**, 1305–1350 (2022).
20. Butt, E. W. et al. Amazon deforestation causes strong regional warming. *Proc. Natl Acad. Sci. USA* **120**, e2309123120 (2023).
21. Bala, G. et al. Combined climate and carbon-cycle effects of large-scale deforestation. *Proc. Natl Acad. Sci. USA* **104**, 6550–6555 (2007).
22. Williams, C. A., Gu, H. & Jiao, T. Climate impacts of U.S. forest loss span net warming to net cooling. *Sci. Adv.* **7**, eaax8859 (2021).
23. Loarie, S. R., Lobell, D. B., Asner, G. P., Mu, Q. & Field, C. B. Direct impacts on local climate of sugar-cane expansion in Brazil. *Nat. Clim. Change* **1**, 105–109 (2011).
24. Arora, V. K. & Montenegro, A. Small temperature benefits provided by realistic afforestation efforts. *Nat. Geosci.* **4**, 514–518 (2011).

25. Windisch, M. G., Davin, E. L. & Seneviratne, S. I. Prioritizing forestation based on biogeochemical and local biogeophysical impacts. *Nat. Clim. Change* **11**, 867–871 (2021).
26. Kumar, S. et al. Land use/cover change impacts in CMIP5 climate simulations: A new methodology and 21st century challenges. *J. Geophys. Res. Atmos.* **118**, 6337–6353 (2013).
27. Alkama, R. et al. Vegetation-based climate mitigation in a warmer and greener World. *Nat. Commun.* **13**, 606 (2022).
28. He, M. et al. Amplified warming from physiological responses to carbon dioxide reduces the potential of vegetation for climate change mitigation. *Commun. Earth Environ.* **3**, 160 (2022).
29. Cook, B. I., Smerdon, J. E., Seager, R. & Coats, S. Global warming and 21st century drying. *Clim. Dyn.* **43**, 2607–2627 (2014).
30. Yuan, W. et al. Increased atmospheric vapor pressure deficit reduces global vegetation growth. *Sci. Adv.* **5**, eaax1396 (2019).
31. Milly, P. C. D. & Dunne, K. A. Potential evapotranspiration and continental drying. *Nat. Clim. Change* **6**, 946–949 (2016).
32. Ukkola, A. M. et al. Reduced streamflow in water-stressed climates consistent with CO_2 effects on vegetation. *Nat. Clim. Change* **6**, 75–78 (2016).
33. Jasechko, S. Plants turn on the tap. *Nat. Clim. Change* **8**, 562–563 (2018).
34. Van Der Sleen, P. et al. No growth stimulation of tropical trees by 150 years of CO_2 fertilization but water-use efficiency increased. *Nat. Geosci.* **8**, 24–28 (2015).
35. Zhu, Z. et al. Greening of the Earth and its drivers. *Nat. Clim. Change* **6**, 791–795 (2016).
36. Cowling, S. A. & Field, C. B. Environmental control of leaf area production: Implications for vegetation and land-surface modeling. *Glob. Biogeochem. Cycles* **17**, (2003).
37. Donohue, R. J., Roderick, M. L., McVicar, T. R. & Farquhar, G. D. Impact of CO_2 fertilization on maximum foliage cover across the globe's warm, arid environments. *Geophys. Res. Lett.* **40**, 3031–3035 (2013).
38. Liang, X. et al. Stomatal responses of terrestrial plants to global change. *Nat. Commun.* **14**, 2188 (2023).
39. Ainsworth, E. A. & Long, S. P. What have we learned from 15 years of free-air CO_2 enrichment (FACE)? A meta-analytic review of the responses of photosynthesis, canopy properties and plant production to rising CO_2. *N. Phytol.* **165**, 351–372 (2005).
40. Coumou, D., Lehmann, J. & Beckmann, J. The weakening summer circulation in the Northern Hemisphere mid-latitudes. *Science* **348**, 324–327 (2015).
41. Cohen, J. et al. Recent Arctic amplification and extreme mid-latitude weather. *Nat. Geosci.* **7**, 627–637 (2014).
42. Budikova, D. Role of Arctic sea ice in global atmospheric circulation: A review. *Glob. Planet. Change* **68**, 149–163 (2009).
43. Coumou, D., Di Capua, G., Vavrus, S., Wang, L. & Wang, S. The influence of Arctic amplification on mid-latitude summer circulation. *Nat. Commun.* **9**, 2959 (2018).
44. Francis, J. A. & Vavrus, S. J. Evidence linking Arctic amplification to extreme weather in mid-latitudes. *Geophys. Res. Lett.* **39**, 2012GL051000 (2012).
45. Dufresne, J.-L. et al. Climate change projections using the IPSL-CM5 Earth System Model: from CMIP3 to CMIP5. *Clim. Dyn.* **40**, 2123–2165 (2013).
46. Marti, O. et al. Key features of the IPSL ocean atmosphere model and its sensitivity to atmospheric resolution. *Clim. Dyn.* **34**, 1–26 (2010).
47. Bastin, J.-F. et al. The global tree restoration potential. *Science* **365**, 76–79 (2019).
48. O'Neill, B. C. et al. The Scenario Model Intercomparison Project (ScenarioMIP) for CMIP6. *Geosci. Model Dev.* **9**, 3461–3482 (2016).
49. Harper, K. L. et al. A 29-year time series of annual 300 m resolution plant-functional-type maps for climate models. *Earth Syst. Sci. Data* **15**, 1465–1499 (2023).
50. Badger, A. M. & Dirmeyer, P. A. Remote tropical and sub-tropical responses to Amazon deforestation. *Clim. Dyn.* **46**, 3057–3066 (2016).
51. Zeng, Z. et al. Climate mitigation from vegetation biophysical feedbacks during the past three decades. *Nat. Clim. Change* **7**, 432–436 (2017).
52. Betts, A. K. & Ball, J. H. Albedo over the boreal forest. *J. Geophys. Res.* **102**, 28901–28909 (1997).
53. Xu, R. et al. Contrasting impacts of forests on cloud cover based on satellite observations. *Nat. Commun.* **13**, 670 (2022).
54. Cerasoli, S., Yin, J. & Porporato, A. Cloud cooling effects of afforestation and reforestation at midlatitudes. *Proc. Natl Acad. Sci. USA* **118**, e2026241118 (2021).
55. Duveiller, G. et al. Revealing the widespread potential of forests to increase low level cloud cover. *Nat. Commun.* **12**, 4337 (2021).
56. Chen, C. et al. Biophysical impacts of Earth greening largely controlled by aerodynamic resistance. *Sci. Adv.* **6**, eabb1981 (2020).
57. Winckler, J., Reick, C. H., Bright, R. M. & Pongratz, J. Importance of Surface Roughness for the Local Biogeophysical Effects of Deforestation. *J. Geophys. Res. Atmos.* **124**, 8605–8618 (2019).
58. Su, Y. et al. Asymmetric influence of forest cover gain and loss on land surface temperature. *Nat. Clim. Change* **13**, 823–831 (2023).
59. Lejeune, Q., Davin, E. L., Gudmundsson, L., Winckler, J. & Seneviratne, S. I. Historical deforestation locally increased the intensity of hot days in northern mid-latitudes. *Nat. Clim. Change* **8**, 386–390 (2018).
60. Roebroek, C. T. J. et al. Potential tree cover under current and future climate scenarios. *Sci. Data* **12**, 564 (2025).
61. Chylek, P. et al. Annual Mean Arctic Amplification 1970–2020: Observed and Simulated by CMIP6 Climate Models. *Geophys. Res. Lett.* **49**, e2022GL099371 (2022).
62. Previdi, M., Smith, K. L. & Polvani, L. M. Arctic amplification of climate change: a review of underlying mechanisms. *Environ. Res. Lett.* **16**, 093003 (2021).
63. Screen, J. A. Arctic amplification decreases temperature variance in northern mid- to high-latitudes. *Nat. Clim. Change* **4**, 577–582 (2014).
64. Devaraju, N., De Noblet-Ducoudré, N., Quesada, B. & Bala, G. Quantifying the relative importance of direct and indirect biophysical effects of deforestation on surface temperature and teleconnections. *J. Clim.* **31**, 3811–3829 (2018).
65. Devaraju, N., Bala, G. & Nemani, R. Modelling the influence of land-use changes on biophysical and biochemical interactions at regional and global scales. *Plant Cell Environ.* **38**, 1931–1946 (2015).
66. Swann, A. L. S., Fung, I. Y. & Chiang, J. C. H. Mid-latitude afforestation shifts general circulation and tropical precipitation. *Proc. Natl Acad. Sci. USA* **109**, 712–716 (2012).
67. Hoskins, B. J. & Karoly, D. J. The steady linear response of a spherical atmosphere to thermal and orographic forcing. *J. Atmos. Sci.* **38**, 1179–1196 (1981).
68. Snyder, P. K. The influence of tropical deforestation on the northern hemisphere climate by atmospheric teleconnections. *Earth Interact.* **14**, 1–34 (2010).
69. Devaraju, N., Tharammal, T. & Bala, G. Biophysical and biogeochemical effects of historical and future scenarios of anthropogenic land cover change on climate. Preprint at https://doi.org/10.21203/rs.3.rs-2292826/v1 (2022).
70. Hourdin, F. et al. The LMDZ4 general circulation model: climate performance and sensitivity to parametrized physics with emphasis on tropical convection. *Clim. Dyn.* **27**, 787–813 (2006).
71. Li, Z.-X. Ensemble atmospheric GCM simulation of climate interannual variability from 1979 to 1994. *J. Clim.* **12**, 986–1001 (1999).

72. Krinner, G. et al. A dynamic global vegetation model for studies of the coupled atmosphere-biosphere system. *Glob. Biogeochem. Cycles* **19**, 2003GB002199 (2005).
73. Lian, X. et al. Biophysical impacts of northern vegetation changes on seasonal warming patterns. *Nat. Commun.* **13**, 3925 (2022).
74. Li, Y. et al. Divergent hydrological response to large-scale afforestation and vegetation greening in China. *Sci. Adv.* **4**, eaar4182 (2018).
75. Lian, X. et al. Partitioning global land evapotranspiration using CMIP5 models constrained by observations. *Nat. Clim. Change* **8**, 640–646 (2018).
76. Meinshausen, M. et al. Historical greenhouse gas concentrations for climate modelling (CMIP6). *Geosci. Model Dev.* **10**, 2057–2116 (2017).
77. Meinshausen, M. et al. The shared socio-economic pathway (SSP) greenhouse gas concentrations and their extensions to 2500. *Geosci. Model Dev.* **13**, 3571–3605 (2020).
78. Lawrence, D. M. et al. The land use model intercomparison project (LUMIP) contribution to CMIP6: rationale and experimental design. *Geosci. Model Dev.* **9**, 2973–2998 (2016).

Acknowledgements

This study was supported by the Second Tibetan Plateau Scientific Expedition and Research (STEP) program (2024QZKK0301), the National Natural Science Foundation of China (41988101). This work was also supported by the Peking University-BHP Carbon and Climate Wei-Ming Phd Scholars Program (Grant No. WM202304 for H.X. and Grant No. WM202411 for F.K.). J.P. was supported by the Catalan Government grant (SGR AGAUR2023 CLIMA 00118) and the European Union grant CONCERTO (HORIZON-CL5-2024-D1-01). The analysis and calculations were supported by High-performance Computing Platform of Peking University.

Author contributions

S.P., X.L., and H.X. designed the research. X.L., H.X., and F.K. performed the simulation. F.K. performed the analysis. F.K., H.X., X.L., and J.P. drafted the paper. C.T.J.R. provided additional tree cover capacity data for the sensitivity test. S.T., C.T.J.R., N.A., and K.W. commented on the manuscript. All authors contributed to the interpretation of the results and to the text.

Competing interests

The authors declare no competing interests.

Additional information

Supplementary information The online version contains supplementary material available at https://doi.org/10.1038/s41467-025-59547-y.

Correspondence and requests for materials should be addressed to Hao Xu or Shilong Piao.

Peer review information *Nature Communications* thanks Narayanappa Devaraju, Gregory Duveiller, Raphael Portmann, and the other, anonymous, reviewer for their contribution to the peer review of this work. A peer review file is available.

Reprints and permissions information is available at http://www.nature.com/reprints